



HAL
open science

Continuous monitoring of surface optical properties across a geostrophic front: Biogeochemical inferences

Hervé Claustre, Frank Fell, Kadija Oubelkheir, Louis Prieur, Antoine Sciandra, Bernard Gentili, Marcel Babin

► **To cite this version:**

Hervé Claustre, Frank Fell, Kadija Oubelkheir, Louis Prieur, Antoine Sciandra, et al.. Continuous monitoring of surface optical properties across a geostrophic front: Biogeochemical inferences. *Limnology and Oceanography*, 2000, 45 (2), pp.309 - 321. 10.4319/lo.2000.45.2.0309 . hal-01893882

HAL Id: hal-01893882

<https://hal.science/hal-01893882>

Submitted on 6 May 2021

HAL is a multi-disciplinary open access archive for the deposit and dissemination of scientific research documents, whether they are published or not. The documents may come from teaching and research institutions in France or abroad, or from public or private research centers.

L'archive ouverte pluridisciplinaire **HAL**, est destinée au dépôt et à la diffusion de documents scientifiques de niveau recherche, publiés ou non, émanant des établissements d'enseignement et de recherche français ou étrangers, des laboratoires publics ou privés.



Distributed under a Creative Commons Attribution 4.0 International License

Continuous monitoring of surface optical properties across a geostrophic front: Biogeochemical inferences

Hervé Claustre¹, Frank Fell, Kadija Oubelkheir, and Louis Prieur

Laboratoire de Physique et Chimie Marines, CNRS-INSU et Université Pierre et Marie Curie, B.P. 08, 06238 Villefranche-sur-mer, France

Antoine Sciandra

Laboratoire d'Océanographie Biologique et Ecologie du Plancton Marin, CNRS-INSU et Université Pierre et Marie Curie, B.P. 28, 06238 Villefranche-sur-mer, France

Bernard Gentili and Marcel Babin

Laboratoire de Physique et Chimie Marines, CNRS-INSU et Université Pierre et Marie Curie, B.P. 08, 06238 Villefranche-sur-mer, France

Abstract

A system was designed for the continuous surface monitoring of hydrological, bio-optical, and biogeochemical properties in the vicinity of the Almeria-Oran jet-front system (Northwestern Mediterranean Sea). This system included a thermosalinograph, a fluorometer, an optical particle counter, and an absorbance-attenuance meter (AC9), allowing the estimation of the absorption [$a(\lambda)$, (m^{-1})] and scattering [$b(\lambda)$, (m^{-1})] coefficients at nine wavelengths. More than 500 multivariate records were acquired over a transect crossing the jet-front system three times and encompassing the diversity of water types encountered in this area. A method is proposed to retrieve relevant biogeochemical or bio-optical quantities, among which are the chlorophyll *a* concentration [from $a(676)$], the particulate carbon concentration [from $b(555)$], the colored dissolved organic matter [CDOM, from $a(412)$], and the chlorophyll-specific scattering coefficient at 555 nm, $b^*(555)$ ($\text{m}^2 \text{ mg Chl } a^{-1}$). The analyses of these various quantities with respect to the surface hydrodynamic fields reveal two main features. First, the particle pool displays highly dynamic quantitative variations across the frontal structure. Qualitatively, flagellate-dominated populations are associated with moderate density waters and maximal jet velocity, while diatoms are recorded at the narrow limit between the jet-front and the Mediterranean waters, where jet velocity is minimal. Second, the CDOM pool presents remarkable covariations with the surface-density field. In particular, the lowest $a_{\text{CDOM}}(412)$ values are reproducibly associated with the highest density values, which track upwelled flow associated with the frontal circulation; accumulation of CDOM is always observed inside the frontal waters, at a density value of 27.2 kg m^{-3} . These CDOM variations suggest that the frontal system is the place of enhanced biological activity.

Hydrodynamics drive the distribution of phytoplankton in the light and nutrient fields. This forcing determines the productivity of a system, its trophic status, and finally the cycle of biogenic elements. To describe these properties, a proper sampling strategy requires simultaneous description of the physical and biogeochemical fields. For observation conducted at small scale, such a statement is far from being trivial: observations of biogeochemical fields are generally based on measurements performed on discrete samples, and thus cannot be conducted at the same resolution as obser-

vations of physical fields. Therefore, alternative strategies have to be developed to fit the requirements of biogeochemical studies at small scales.

The use of continuous profilers, as many of them are becoming available to the oceanographic community, offers an alternative solution. Among these instruments, fluorometers and transmissometers are widely used for bulk descriptions of the particulate pool (e.g., Chung et al. 1998; Claustre et al. 1999). To be useful in a biogeochemical sense, chlorophyll *a* (Chl *a*) fluorescence measurements have to be converted into Chl *a* concentration (e.g., Strass 1990), while the attenuation coefficient, derived from transmission measurements, has to be converted into particulate carbon (PC) equivalents (e.g., Loisel and Morel 1998; Bishop 1999).

Recently, new generations of spectral absorptiometers and transmissometers have been used to monitor spatial (Barth et al. 1998) and temporal (Dickey et al. 1998) changes in bio-optical properties. The spectral information may allow retrieval of specific biogeochemical quantities. Indeed, some of these quantities (e.g., vegetal matter, particulate matter, detritus, colored dissolved organic matter) are optically significant substances: they modify the light field according to their absorption and/or scattering properties. The qualitative

¹ Corresponding author (claustre@obs-vlfr.fr).

Acknowledgments

We acknowledge the financial support of the EEC Coast/ooc program (contract ENV4-CT96-0310), of Frontal-ALMOFRONT, PROSOPE, and DYFAMED operations of the PROOF-program and of the CNRS "Direction des Relations Internationales." Kadija Oubelkheir received a CNRS and Région PACA fellowship. We thank Anabelle Cuttelod for the calibrations of the Seatech transmissometer and fluorometer in POC and chlorophyll *a* concentrations, respectively. Patrick Chang is thanked for fine tuning the English. Annick Bricaud and two anonymous reviewers are acknowledged for constructive criticisms.

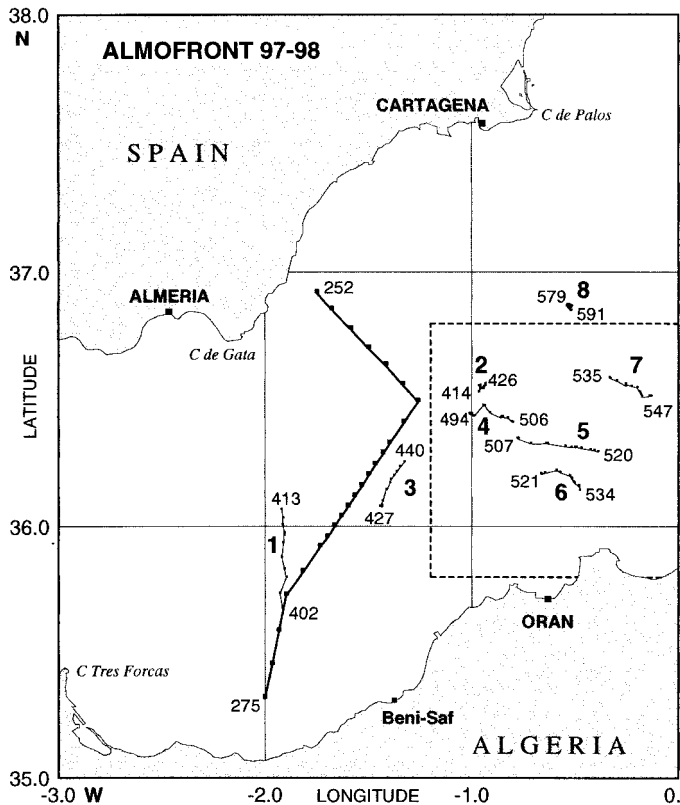


Fig. 1 General map of area investigated during the Almofront II cruise in the Alboran Sea. For each of the eight 2-d sites (leg 2), the number of the first and last CTD casts are shown in order to highlight the general drift. The inset (dashed line) corresponds to the area where the transect analyzed in this paper was conducted (see Fig. 2).

(spectral) modifications of light are specific to the substance, while the quantitative modifications are related to the concentration of the substance. The development of deconvolution procedures for the in situ retrieval and estimation of biogeochemical descriptors is a major challenge for deriving optimal information from available (and forthcoming) bio-optical instrumentation.

As a part of the French Frontal-Joint Global Ocean Flux Study (JGOFS) program, the main goal of the Almofront II cruise was to understand the coupling between physics and biogeochemistry at the scale of a geostrophic frontal system, the Almeria-Oran front. This front results from the abutting of surface Atlantic and Mediterranean waters in the Alboran Sea. Previous investigations have evidenced strong biogeochemical signatures associated with this frontal system (Claustre et al. 1994b; Peinert and Miquel 1994). These investigations were mainly conducted using classical sampling strategies associated with standard methodologies; they were not able to resolve small-scale biogeochemical features, in particular those associated with cross-frontal circulation. The specific goal of the present investigation was to study the coupling between physical and biogeochemical processes at mesoscales (10 km) and submesoscales (~1 km). In this context, we developed a device to continuously monitor surface hydrological and bio-optical properties and a method

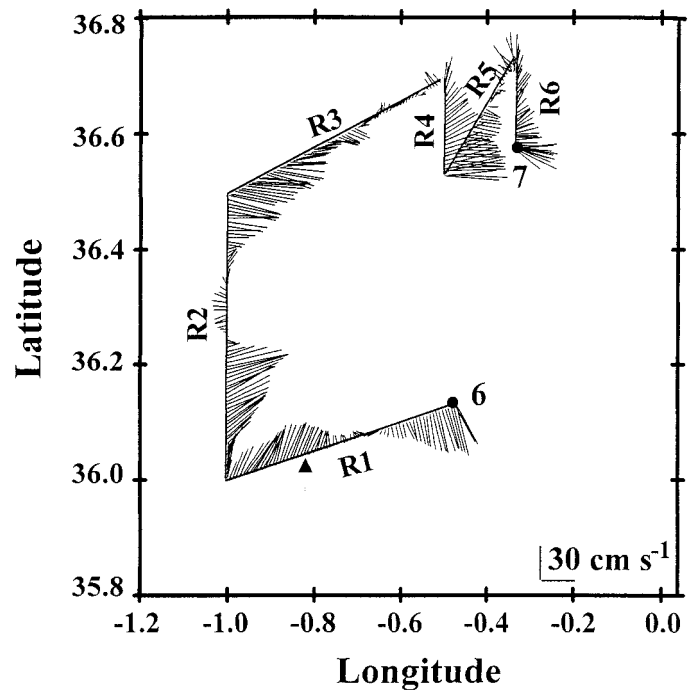


Fig. 2 Map of the transect and transect surface currents. The transect began on 7 January (1600 h) at site 6 and ended on 8 January (0330 h) at site 7. R1 to R6 refer to the various subsections. The arrow refers to the position where the multivariate acquisition began. The scale of the velocity vectors is shown on the bottom right corner of the figure.

allowing the retrieval of biogeochemically relevant quantities. The variations of these quantities are analyzed in the context of our current knowledge on circulation associated with geostrophic fronts.

Materials and methods

General context—Investigations were conducted on board the R.V. *L'Atalante* in the Alboran Sea from 29 November 1997 to 16 January 1998. Leg 1 (ending on 21 December) focused on the hydrological description of the whole area and on the localization of the jet-front system. Two types of investigations were performed during leg 2: (1) Process studies were conducted at eight 36-h sites (Fig. 1), representative of the variety of hydrodynamic and trophic situations encountered during leg 1. They were essentially based on repeated vertical profiles that provided water samples for a variety of bio-optical and biogeochemical measurements, including those used in the present study. (2) Transects at 12 knots provided a surface synoptic description of the area between two consecutive sites. The transect we will refer to in the present study began on 7 January at 1600 h, just after site 6 (Fig. 2). This transect was composed of six subsections (R1 to R6) of different directions (Fig. 2) and was completed on arrival at site 7 on 8 January at 0330 h.

Continuous data acquisition and processing—ADCP: Current data were recorded with a 300-kHz vessel-mounted

RDI® acoustic Doppler current profiler (ADCP). Data were georeferenced and averaged over 2 min, corresponding to approximately 200 pings. Absolute velocities were determined from the ship position as given by the precise differential (70 cm) global positioning system (GPS) every 2 min. The data presented in Fig. 2 correspond to current velocities between 24 and 28 m.

Other variables were measured from seawater pumped from 4 m below the ship's hull. On board, the seawater flowed through a thermosalinograph and a fluorometer. Then, after degassing in a 1-liter chamber, water was dispatched to an absorbance-attenuance meter and a particle counter. Owing to the combination of pipe length, dead volumes, and flow rate, the water took 6 min to reach the laboratory instruments. The time of laboratory measurements was therefore accordingly shifted to match the real-time ADCP measurements.

Thermosalinograph data: A SBE 21 Seabird thermosalinograph monitored temperature and salinity. Owing to the time spent inside the ship (*see above*) the thermosalinograph temperature was about 0.6°C higher than the temperature measured in situ by a quartz thermograph at the ship's bow. Therefore only in situ temperature was included in the data. Data were subsequently binned over a 1-min interval, which corresponds to a distance of approximately 370 m for a ship speed of 12 knots.

Fluorescence data: A Turner Design (model 10 AU) fluorometer was used to monitor the Chl *a* fluorescence variations. Data were binned over 1-min intervals. Postexamination of the signal highlighted periods of unexpected decrease below the background signal. The corresponding data were discarded. The fluorescence data are expressed in relative units.

Spectral absorption and attenuation: Continuous measurements (6 Hz) of the absorption [$a(\lambda)$] and attenuation [$c(\lambda)$] coefficients were conducted at nine wavelengths (412, 440, 488, 510, 532, 555, 630, 676, and 715 nm) using a flow-through in situ absorbance-attenuance meter (AC9®, Wetlabs) connected to the seawater line. As the measurements are referenced to pure (Milli-Q) water, the obtained absorption and attenuation coefficients exclude the contribution of water. Data were acquired using the Wetview® (Wetlabs) software and binned over 1-min intervals. The variations in temperature (16.2–17.8°C, given by the laboratory thermograph) and in salinity (36.6–37.7 PSU) recorded during the transect were minor regarding their potential effect on absorption and attenuation by pure water (Pegau et al. 1997). Therefore $a(\lambda)$ and $c(\lambda)$ data were postprocessed for temperature and salinity correction using constant values of 17°C and 37 PSU, respectively. To correct absorption measurements for incomplete recovery of scattered light, $a(715)$ was subtracted from $a(\lambda)$. Temporal drifts recorded in the a and c signal, likely resulting from the accumulation of biogenic material and/or small bubbles on the windows and tubes, were corrected using an exponential detrending. The efficiency of this procedure was tested by checking the signal stability when the ship was on site (the last 3 h of data acquisition) and where

a steady signal was expected, as was observed for particle abundance or in vivo fluorescence. Finally, the scattering coefficient, $b(\lambda)$, was derived through: $b(\lambda) = c(\lambda) - a(\lambda)$. As the contribution of molecular (water) scattering is excluded (*see above*), this coefficient essentially corresponds to particle scattering and is hereafter denoted $b_p(\lambda)$.

Size spectra: The particle size distributions in the range 1.7–100 μm within 200 log-normally distributed size intervals were determined using an Hiac/Royco particle counter (Pacific Scientific). The measurement is based on the light blockage principle. The sampling device was connected to the 1-liter chamber and the flow rate through the sensor was maintained at 25 ml min⁻¹. Size spectra and particle concentrations were automatically obtained every 48 s from 20-ml samples. Postcruise laboratory measurements performed on seawater and different phytoplankton strains including diatoms, coccolithophorids, and cryptophytes have shown that size spectra recorded in the range 1.7–10 μm by the Hiac sizer agree within 1 to 10% with Coulter counter (Multisizer II) estimates.

A scattering coefficient, $b_p^h(\lambda)$, was derived from Hiac measurements and using the Mie theory for particles assumed to be spherical and to have a relative index of refraction, n , of 1.05. The computation was performed on two data sets. The first one corresponds to the size distributions (1.7–30 μm) obtained directly from Hiac measurements. The second data set is obtained by extending the measured size distribution toward small particles (0.1 μm) by assuming a size distribution function of the Junge type having a -4.5 exponent.

Discrete data acquisition and processing—At the sites, water samples were taken from a 24-bottle rosette coupled to a Seabird conductivity-temperature-depth (CTD), a Seatech transmissiometer, and a Seatech Fluorometer. These samples were analyzed to derive the following quantities:

Particulate absorption: 2.8 liters of seawater were filtered through a Whatman GF/F glass-fiber filter, and optical densities of the particles were measured, between 370 and 750 nm in 1-nm increments, using a LICOR radiometer (LI-1800 UW) equipped with an integrating sphere. The particle absorption coefficient was derived using a parameterization of the path length amplification factor given by Mitchell and Kiefer (1988). Finally, the numerical decomposition procedure of Bricaud and Stramski (1990) was applied to the particle absorption coefficient in order to estimate the phytoplankton and the nonphytoplankton absorption coefficients.

Pigments: High-pressure liquid-chromatography (HPLC) pigment analyses (Vidussi et al. 1996) were performed on board on the samples used for absorption determination. Just after optical measurements, filters were put into vials containing 3 ml of MeOH and a known amount of Zn(II) pyropheophorbide *a* octadecyl ester as internal standard, and stored at -80°C for at least 2 h. Extraction was completed using a sonication probe and filtrates clarified by filtration onto GF/C glass-fiber filters.

Particulate carbon: 2.8 liters were filtered onto GF/F previously cleaned in a Soxhlet extractor with dichloromethane (Claustre et al. 1999). Particulate carbon (PC) was analyzed in the laboratory, less than 2 months after the end of the cruise, using an LECO® 900 carbon analyzer with ethylenediaminetetraacetic acid (EDTA) as a standard.

Background: biogeochemical inferences from the present measurements

Inferences from absorption measurements—Three major biogenic pools contribute to variations in the absorption coefficient in oceanic areas: the phytoplankton (ϕ), the colored dissolved organic matter (CDOM), and the nonalgal particles (NAP, including detritus and nonpigmented cells), (e.g., Bricaud et al. 1981, 1995; Prieur and Sathyendranath 1981). Their contributions are additive, so that $a(\lambda)$ can be expressed as:

$$a(\lambda) = a_{\text{CDOM}}(\lambda) + a_{\text{NAP}}(\lambda) + a_{\phi}(\lambda). \quad (1)$$

Note that $a(\lambda)$ represents the total absorption coefficient minus the absorption coefficient of pure water; see Materials and methods.

The spectral shapes of $a_{\text{CDOM}}(\lambda)$ and $a_{\text{NAP}}(\lambda)$ are very similar, which makes the two pools hardly distinguishable on the basis of their absorption properties (e.g., Roesler et al. 1989). Acknowledging this, some studies therefore refer to a single colored detrital matter (CDM) pool (e.g., Siegel and Michaels 1996) such that:

$$a_{\text{CDM}}(\lambda) = a_{\text{NAP}}(\lambda) + a_{\text{CDOM}}(\lambda). \quad (2)$$

Absorption due to phytoplankton: At 676 nm, the absorption due to CDM can be considered as negligible in oceanic waters. Therefore, $a(676)$ is primarily an estimation of the absorption by phytoplankton, hereafter denoted $a_{\phi}(676)$, and can be used to estimate chlorophyll concentration [$\langle\text{Chl}\rangle$, in mg m^{-3}]. A relationship between measured $\langle\text{Chl}\rangle$ and $a_{\phi}(676)$ was established on the basis of discrete measurements (Fig. 3A):

$$\langle\text{Chl}\rangle = 136a_{\phi}(676)^{1.24}. \quad (3)$$

The choice of a power-law function allows us to take into consideration the decrease of the chlorophyll-specific absorption coefficient as a function of increasing $\langle\text{Chl}\rangle$ concentration, likely the result of packaging effect. For the range of $a_{\phi}(676)$ values considered here, this parameterization is similar to that derived from Bricaud et al. (1995), which was established on a global and extensive data set (Fig. 3A).

Absorption due to CDOM and NAP: In the present investigation, $a(412)$ is the most appropriate and sensitive measurement to study the dynamics of the CDM pool because of the well-known $a_{\text{CDM}}(\lambda)$ increase with decreasing wavelengths (e.g., Roesler et al. 1989, and references therein). However, in order to estimate $a_{\text{CDM}}(412)$, the contribution of phytoplankton to absorption at 412 nm, $a_{\phi}(412)$, has to be subtracted from $a(412)$ (see Eqs. 1 and 2). The parameter $a_{\phi}(412)$ was estimated on the basis of the discrete measurements, through the relationship presented in Fig. 3B:

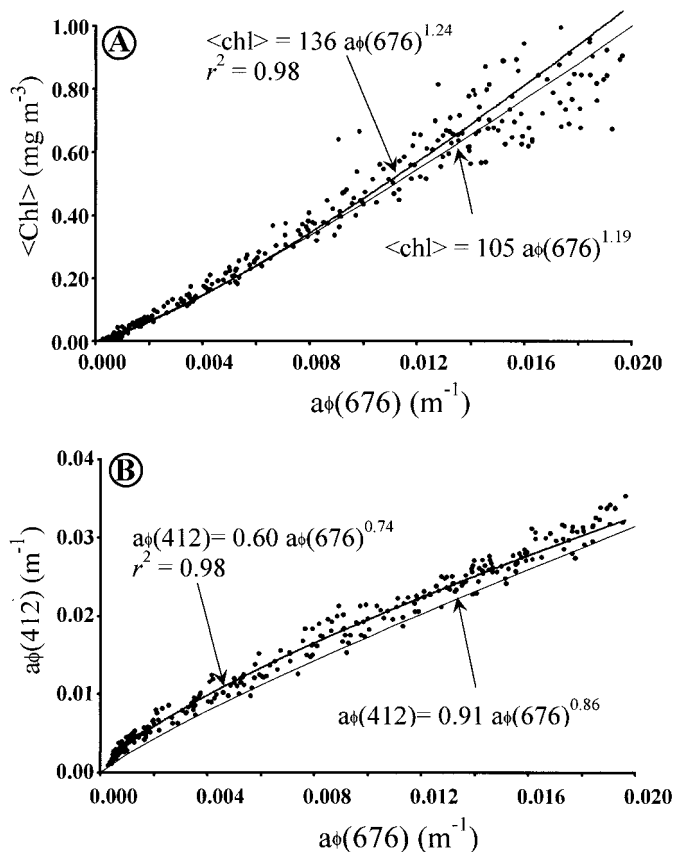


Fig. 3 Statistical relationship used for the retrieval of some bio-optical or biogeochemical variables. (A) HPLC-measured $\langle\text{Chl}\rangle$ vs. $a_{\phi}(676)$ (B) $a_{\phi}(412)$ vs. $a_{\phi}(676)$. The data set used to establish these relationships is restricted to the measurements performed in the transect zone (sites 2, 4, 5, 6, and 7; see Fig. 1 and Materials and methods) and to $a_{\phi}(676)$ values below 0.02 m^{-1} , which correspond to the upper range of measured $a_{\phi}(676)$ during the transect (see Figs. 5, 6). The thick line corresponds to the best fit of the power-law function. The thin line corresponds to the power-law function derived from the parameterization of Bricaud et al. (1995).

$$a_{\phi}(412) = 0.60a_{\phi}(676)^{0.74}. \quad (4)$$

Here again, the power-law expression accounts for the decrease in the blue-to-red ratio of phytoplankton absorption with increasing vegetal biomass as a result of spectral flattening (packaging effect) and of variations in the relative concentration of accessory pigments. In the restricted range of absorption values examined here, the established relationship ends at a higher blue-to-red ratio than for the relationship derived from the global data set of Bricaud et al. (1995) (Fig. 3B).

Equation 4 can now be reintroduced in Eqs. 1 and 2, such that:

$$a_{\text{CDM}}(412) = a(412) - 0.60a_{\phi}(676)^{0.74}. \quad (5)$$

Subsequently, the percentage contribution of CDM to absorption at 412 nm [%CDM(412)] can be defined as

$$\% \text{CDM}(412) = 100a_{\text{CDM}}(412)/a(412). \quad (6)$$

From the data set used to establish Eqs. 3 and 4, the ratio

$a_{\text{NAP}}(412)/a_{\phi}(412)$ was determined on a subset restricted to the 48 surface (0–15 m) samples because this ratio is strongly depth dependant (increase of detritus with depth). Its average value was 0.34 (standard deviation = 0.09). Therefore, it is straightforward that

$$a_{\text{NAP}}(412) = 0.34a_{\phi}(412) = 0.34 \times 0.60a_{\phi}(676)^{0.74}. \quad (7)$$

Finally, rearranging Eqs. 1, 4, and 7 leads to the estimation of CDOM through:

$$a_{\text{CDOM}}(412) = a(412) - 0.80a_{\phi}(676)^{0.74}. \quad (8)$$

No discrete measurement of $a_{\text{CDOM}}(412)$ was performed during this cruise that would have allowed us to perform a definitive validation of the estimated values. However, several pieces of evidence suggest that (1) the retrieval procedure is robust and (2) the absolute values are accurate. First, when the ratio $a_{\text{NAP}}(412)/a_{\phi}(412)$ varies between 0.25 or 0.43 (i.e., average value \pm one standard deviation), the resulting estimate of $a_{\text{CDOM}}(412)$ differs by less than 10% from the estimation obtained from a value of 0.34 (as used in Eq. 7). Moreover, because the nonlinear dependence of $a_{\phi}(412)$ on $a_{\phi}(676)$ is taken into consideration through Eq. 4, the retrieval of $a_{\text{CDOM}}(412)$ is independent of any change in the blue-to-red ratio of phytoplankton absorption. The total independence between $a_{\text{CDOM}}(412)$ and $a_{\phi}(676)$ variation was confirmed on the 537 continuous data acquired during this study ($r^2 = 0.06$; see also later Figs. 5, 6). Second, vertical AC9 profiles performed on the sites (data not shown) allowed us to verify that the $a_{\text{CDOM}}(412)$ estimates were accurate: $a_{\text{CDOM}}(412)$ estimated through Eq. 8 or measured with an AC9 equipped with a 0.2- μm filter [$a_{\text{CDOM}}(412)_f$] were in good agreement [$a_{\text{CDOM}}(412) = 1.28a_{\text{CDOM}}(412)_f - 0.011$; $n = 414$; $r^2 = 0.73$; $p < 0.001$].

Using the above-described deconvolution procedure, an average absorption budget performed at 412 nm shows that phytoplankton, NAP, and CDOM contribute to 33%, 11%, and 56% of $a(412)$, respectively. Furthermore, at the same wavelength, it is found that CDOM is the main contributor of the CDM pool (83%), while NAP contributes only for 17%.

Inferences from scattering measurements—Theoretical and laboratory studies have demonstrated that particles with diameters less than 10 μm account for most of the scattering in oceanic waters (e.g., Morel 1973; Stramski and Kiefer 1991). Therefore, measurements of $b_p(\lambda)$, generally derived from $c_p(\lambda)$ measurements (the subscript p refers to particles), have been subsequently used as an index of particle load in this size range (e.g., Baker and Lavelle 1984; Kitchen and Zaneveld 1990). Here, we have chosen $b_p(555)$ as representative of particle load because 555 nm is in the spectral domain where algal absorption is generally small and where scattering budgets are often performed (e.g., Morel and Ahn 1991; Stramski and Kiefer 1991).

Several studies have attempted to establish a relationship between particulate organic carbon (POC) and particulate scattering (or attenuation) coefficients (Loisel and Morel 1998; Bishop 1999). During the eight 36-h site studies (see Fig. 1 and Materials and methods), simultaneous determi-

nation of $c_p(660)$ (from Seatech Transmissiometer) and particulate carbon ($\langle\text{PC}\rangle$ in mg m^{-3}) along vertical profiles allowed such a relationship to be established for the investigated area:

$$\langle\text{PC}\rangle = 409c_p(660) + 35$$

$$(r^2 = 0.62, p < 0.001, n = 187). \quad (9)$$

The comparison between $b_p(555)$ and $c_p(660)$ for quasi-simultaneous (less than 30 min spaced) Seatech transmissiometer and AC9 profiles performed on several occasions (sites 6, 7, and 8; see Fig. 1) results in the relationship:

$$c_p(660) = 1.097b_p(555) - 0.012$$

$$(r^2 = 0.77, p < 0.001, n = 1119). \quad (10)$$

Finally, combining Eqs. 9 and 10 allowed us to get an estimation of particulate carbon concentration from $b_p(555)$ measurements:

$$\langle\text{PC}\rangle = 449b_p(555) + 30.1. \quad (11)$$

The chlorophyll-specific scattering coefficient at 555 nm, $b_p^*(555)$, is obtained through the normalization of $b_p(555)$ to the chlorophyll concentration, derived from $a_{\phi}(676)$ (Eq. 3). Variations in this coefficient are expected to reflect primarily the balance between the relative contributions of vegetal and nonvegetal particles. The second source of variation is due to change in size or chlorophyll content of the phytoplankton assemblage (Morel 1987) or to the presence of the detached coccoliths of coccolithophorids, which are responsible for an enhancement of the scattering coefficient (e.g., Balch et al. 1996).

Results

Hydrological and hydrodynamic conditions along the transect—Two main hydrodynamic structures were crossed during the transect from site 6 to site 7. The first part of the observations (subtransect R1 to the middle of R2 [Fig. 2] and kilometers 0–75 [Fig. 4]) were conducted in low-density ($<27.0 \text{ kg m}^{-3}$) surface waters. Surface salinity did not exceed 36.8 PSU and surface temperature was always $>16.7^\circ\text{C}$. These hydrological conditions are typical of surface-modified Atlantic waters. The analysis of velocities in the 24–28-m layer (Fig. 2), as well as of velocities in a larger layer (10–200 m) and of infrared satellite imagery (data not shown), emphasize the presence of the Atlantic anticyclonic eddy, which was crossed along R1 and at the beginning of R2.

The second part of the transect (75–200 km) encompassed a wider range of density ($26.8\text{--}27.9 \text{ kg m}^{-3}$) and salinity ($36.8\text{--}37.8 \text{ PSU}$) (Fig. 4). This part is typically the area of the density-driven frontal system, which was crossed three times completely and one time partially (at the end of the transect, R6, Fig. 4). The velocities in the 24–28-m layer are dominated by the eastern component, which traces the main direction of the Atlantic jet. This eastern component varies in an opposite manner with the surface-density field (highest

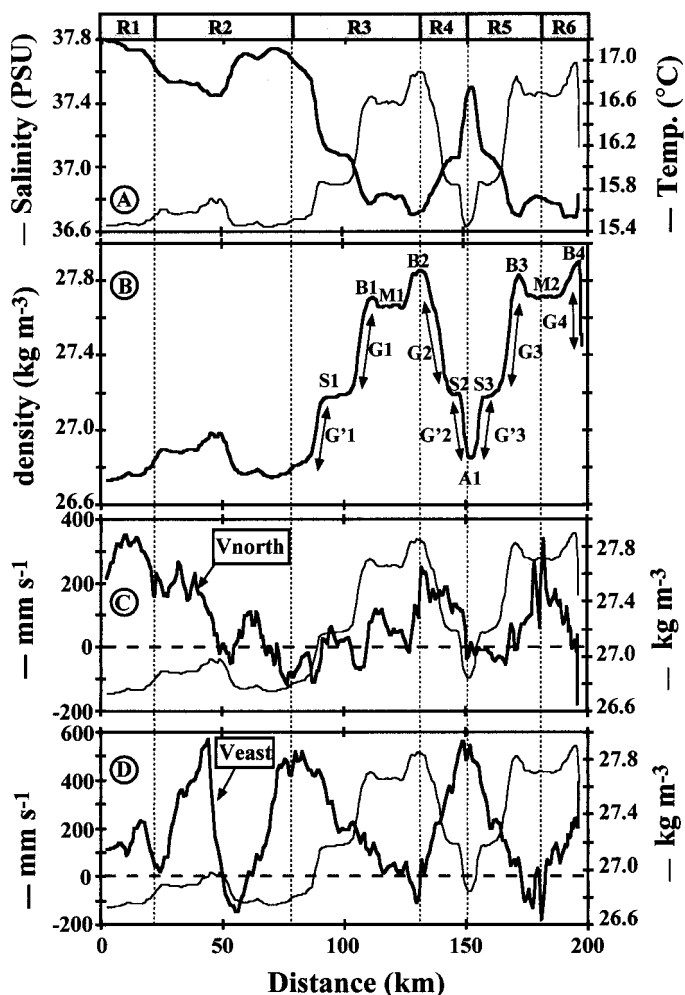


Fig. 4 Hydrological and hydrodynamic characteristics along the transect. (A) Temperature (thick line) and salinity (thin line). (B) Density. The various annotations identify peculiar density patterns described in the text. (C) The north-south component of the current velocities (thick line). The density is superimposed as a thin line. (D) The east-west component of the current velocities (thick line). The density is superimposed as a thin line. The distances are measured from the beginning of the multivariate acquisition (arrow on Fig. 2).

currents associated with low density and reciprocally), which emphasizes that the current core is located on the lighter (Atlantic) side of the surface-density gradient. Moreover, this density gradient from the Atlantic side toward the Mediterranean side is not monotonic: at a σ_θ level of about 27.2 kg m^{-3} , it shows a density step that was crossed three times, hereafter named S1, S2, S3, at kilometers 90, 145, and 155, respectively. On the Atlantic side of each step, the density gradient, crossed three times and hereafter denoted G'1, G'2, and G'3 (Fig. 4), is characterized by eastward velocities always greater than 300 mm s^{-1} . By contrast, on the Mediterranean side, the gradient (crossed four times at G1, G2, G3, and G4) is associated with velocities always lower than 200 mm s^{-1} . Close to the Mediterranean side, and at the end (or the beginning) of G1, G2, G3, and G4, four bumps (B1, B2, B3, B4) are recorded in the density gradients, being likely

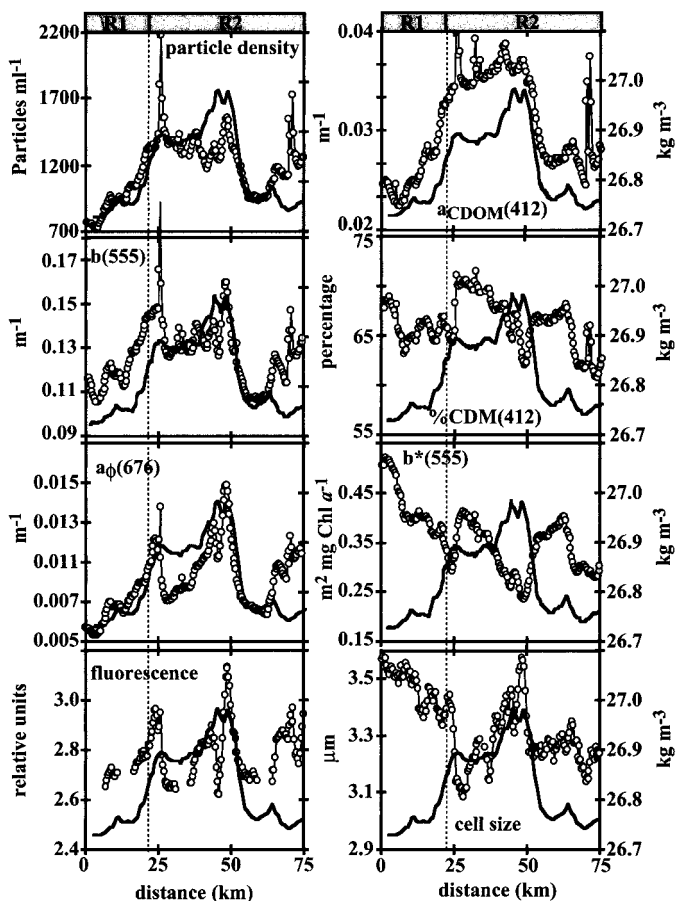


Fig. 5 Bio-optical and biogeochemical patterns along the first part of the transect (0–75 km). Density (thick line) is superimposed on each panel (scale on the right side of the figure). The distances are measured from the beginning of the multivariate acquisition (arrow on Fig. 2).

the result of upwelled flow associated with cross-frontal circulation (Zakardjan and Prieur 1998). Between B1–B2 and B3–B4, the transect explored Mediterranean waters, hereafter called M1 and M2. Finally, the density minimum around kilometer 150 (A1), which also corresponds to a change in the ship direction (transect R4 to R5, Fig. 2), is associated with the core of the jet ($\sim 600 \text{ mm s}^{-1}$ eastward, Fig. 4).

Bio-optical observations along the transect—Owing to the different water masses encountered during the transect, and for the clarity of the presentation, the overall transect will from now be partitioned into two distinct parts. The first part (0–75 km) corresponds to surface Atlantic waters associated with the eddy and the anticyclonic side of the jet. The second part of the transect (75–200 km) begins before G'1 and typically includes the different crossings of the surface-density gradient on the cyclonic side of the jet.

Observations in Atlantic waters: At the beginning of the observations and in waters with a surface density $< 26.75 \text{ kg m}^{-3}$, the lowest values in particle abundance [but not in $b_p(555)$] and in $a_\phi(676)$ were recorded (Fig. 5). Concomi-

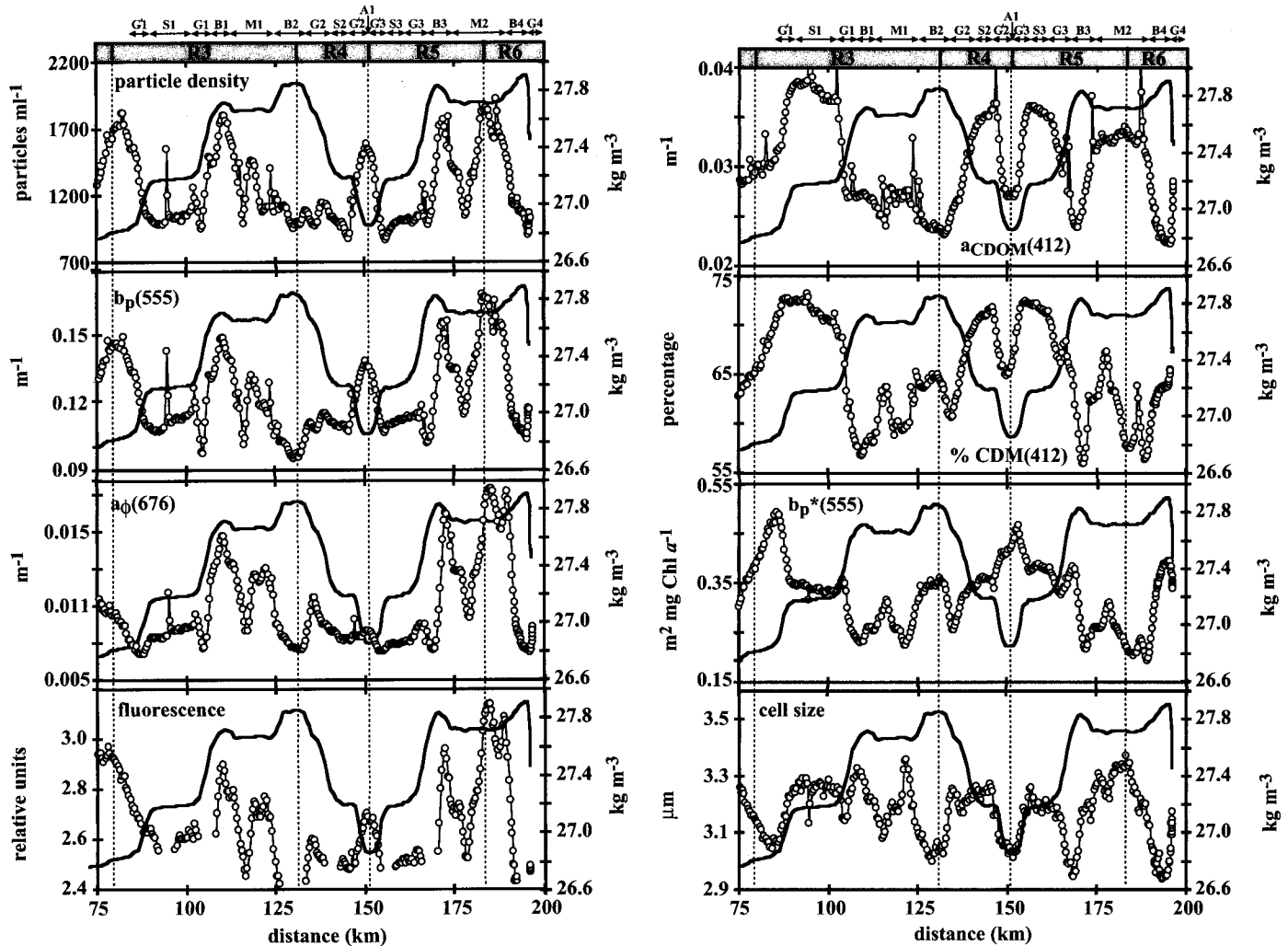


Fig. 6 Bio-optical and biogeochemical patterns along the second part of the transect (75–196 km). Density (thick line) is superimposed on each panel (scale on the right side of the figure). The distances are measured from the beginning of the multivariate acquisition (arrow on Fig. 2).

tantly, $b_p^*(555)$ ($>0.50 \text{ m}^2 \text{ mg Chl } a^{-1}$) and average cell size ($>3.5 \mu\text{m}$) reached their maximal values in this area. For the rest of the transect in the modified Atlantic waters, the variables characterizing changes in concentration of biogenic material, i.e., cell density, $b_p(555)$, $a_p(676)$, fluorescence, $a_{\text{CDOM}}(412)$, and %CDM(412), presented variations that roughly paralleled variations in the surface-density field (Fig. 5). In particular, the weak density gradient starting at kilometer 50 was associated with a sharp decrease in biogenic material. Two (relative) biomass maxima were recorded at kilometers 25 and 50. The second biomass maximum corresponded to an increase in the average particle size and to a relative minimum in $b_p^*(555)$ and in %CDM(412). Finally, the presence of sharp peaks ($<2 \text{ km}$) was noted at kilometers 25 and 70 for cell density, $b_p(555)$, and $a_{\text{CDOM}}(412)$.

Observations across the surface jet-front system: The hydrological (density) and hydrodynamic (e.g., eastern velocity) surface fields were reproducible (Fig. 4) wherever the front-jet system was crossed (Fig. 2). Therefore, the repeti-

tive crossings of this system gave unique opportunities to identify bio-optical or biogeochemical quantities whose variations are driven (or apparently not driven) by these physical fields. Besides the general covariation of variables characterizing the pool of particles [$b_p(555)$ and particle abundance] and of algal material [fluorescence and $a_p(676)$] (Fig. 6), several patterns were observed within the jet-front system area.

The three density steps (S1, S2, S3) were unambiguously associated with the highest $a_{\text{CDOM}}(412)$ values ($>0.35 \text{ m}^{-1}$). As a consequence, they are also the place of the highest contribution in detrital matter [%CDM(412) $>70\%$]. These steps were also associated with rather stable and intermediate values in $b_p^*(555)$ ($0.36\text{--}0.38 \text{ m}^2 \text{ mg Chl } a^{-1}$) and in the average cell size ($\sim 3.2 \mu\text{m}$).

The gradients (G'1, G'2, G'3), starting on the Atlantic side ($\sigma_\theta \sim 26.8 \text{ kg m}^{-3}$) toward the three steps, were associated with a regular increase in $a_{\text{CDOM}}(412)$ and %CDM(412) and with a regular decrease in the particulate pool [$b_p(555)$, particle abundance], as well as in the algal pool [fluores-

cence, $a_{\phi}(676)$]. At kilometers 80 and 150 (A1), corresponding to minimal density values of $\sim 26.8 \text{ kg m}^{-3}$, particle peaks were recorded; they were not reflected by peaks of similar amplitude in $a_{\phi}(676)$ and fluorescence. As a consequence, these locations corresponded to the highest values in $b_p^*(555)$ ($>0.46 \text{ m}^2 \text{ mg Chl } a^{-1}$).

Associated with the gradients (G1–G4) on the Mediterranean part of this transect, $a_{\text{CDOM}}(412)$ and %CDM(412) regularly decreased from the lighter toward the heavier side of the gradient. The responses in other variables were never reproducible from one gradient to another. The same observation also applied to the four density bumps (B1, B2, B3, B4); solely $a_{\text{CDOM}}(412)$ displayed a clear pattern, with the lowest recorded values, especially at B2, B3, and B4 [$a_{\text{CDOM}}(412) < 0.025 \text{ m}^{-1}$]. Finally, on the Mediterranean part of this transect, which was crossed two times (M1 and M2), no parameter displayed a clear response. In particular, $a_{\text{CDOM}}(412)$ is $<0.027 \text{ m}^{-1}$ at M1 and $>0.032 \text{ m}^{-1}$ at M2.

To summarize, several features emerged from the repetitive crossing of the jet-front system. The CDOM pool was the only variable presenting clear and reproducible patterns across the frontal structure, with maxima associated with density steps. These steps defined two zones: in the lighter part, the particle pool reproducibly reacted to the density field; whereas in the heavier part, including the Mediterranean waters, no general pattern could be inferred.

Discussion

Recent advances in instrumentation have allowed the collection of in situ spectral information on optically significant biogenic material; the studies are generally based on time series (Dickey et al. 1998), vertical profiles (Petrenko et al. 1997), or two-dimensional mapping (e.g., Barth et al. 1998) of AC9 measurements. With the same instrumentation, the present investigation is, to our knowledge, the first to provide a continuous record of the spatial variability of the surface bio-optical properties at mesoscale and submesoscale. Moreover, bio-optical data were acquired simultaneously with particle size distribution (range 1.7–30 μm), allowing an evaluation of the dominant particle size classes and a scattering budget to be attempted (*see below*). When compared to classical sampling strategies, based on CTD casts and subsequent sampling for discrete optical and biogeochemical measurements, the present sampling strategy presents several advantages. (1) The perfect coincidence of different measurements [e.g., $a(\lambda)$, $b(\lambda)$, particle abundance] results in a large data set (>500 data) from which statistical inferences can be drawn without ambiguities. (2) Continuous or high-frequency bio-optical acquisitions are the most appropriate way to investigate the coupling between biogeochemical and physical fields at small scales.

In the present study, a full validation of optically derived biogeochemical quantities is not possible because simultaneous discrete measurements were not performed during the transect. However, the range of variation in $\langle \text{Chl} \rangle$ (factor 4: 0.21–0.88 $\text{mg Chl } a \text{ m}^{-3}$) derived from $a_{\phi}(676)$ using Eq. 3 falls within the range of variation of the 66 surface (0–15 m) HPLC–Chl a measurements (0.20–1.19 $\text{mg Chl } a \text{ m}^{-3}$)

performed during the site exploration (*see Fig. 1*). Similarly, the range of variation in $\langle \text{PC} \rangle$ (factor 1.6: 74–119 mg C m^{-3}) derived from $b_p(555)$ using Eq. 11 is within the range of the 25 $\langle \text{PC} \rangle$ discrete surface measurements (66–137 mg C m^{-3}).

Comparison of independent measurements—The present investigation is, to our knowledge, the first where simultaneous determinations of the scattering coefficient and particle size distribution and density are performed on natural samples at small scale. The significant ($p < 0.001$) covariation between the AC9-measured $b_p(555)$ and particle density in the size range 1.7–30 μm confirms that the scattering coefficient (here at 555 nm) is a good proxy of particle load (Fig. 7A). The relationship between measured and computed scattering coefficient [$b_p^h(555)$ determined from the density and the size distribution of these particles using Mie theory; *see Materials and methods*] is slightly better than the relationship between particle density and $b_p(555)$ (compare r^2 values for Fig. 7A,B). This result points out that, beside the density of the particles, their size is a second-order driver of the scattering coefficient. Figure 7B nevertheless highlights that particles in the size range 1.7–30 μm do not explain all the measured $b_p(555)$ coefficient, which is in agreement with theoretical studies that predict that 40–60% of scattering is due to particles $<2 \mu\text{m}$ (assuming a size distribution of the Junge type with an exponent in the range -4 to 4.5 , and a relative refractive index, n , of 1.05). However, when the particles not enumerated by the Hiac counter (0.1–1.7 μm) are taken into consideration (*see Materials and methods*), a large part of measured $b_p(555)$ still remains unexplained (Fig. 7C). Several reasons can be advanced for such discrepancies. First, some systematical errors associated with each measurement (e.g., evaluation of the size distribution by the counter, scattering correction for a when b is calculated through $c - a$), although difficult to quantify, cannot be discarded. Another source of discrepancy involves the necessary assumption concerning the optical parameterization of the particles (sphericity, $n = 1.05$), which is here considered as constant over the range 0.1–30 μm . Finally the choice of the type of the size distribution for particles in the range 0.1–1.7 μm is important. In the 1.7–30 μm range (enumerated by the Hiac counter), the size distribution of particles can be roughly approximated by a power law of exponent -3 . This emphasizes the relative importance (in terms of concentration and subsequently in terms of scattering) of large particles compared to the small ones when these last are approximated using a power-law function of the Junge type with a -4.5 exponent. Such an exponent value is considered as standard (e.g., Morel and Ahn 1991; Stramski and Kiefer 1991), although some previous studies (Brown and Gordon 1974) have reported a Junge exponent of -6 for small particles (0.65–1 μm). Therefore, the discrepancy revealed by Fig. 7C using a standard parameterization likely points to possible optical and size distribution singularities of the picoparticles and, in particular, of picodetritus whose significant role in scattering has recently been emphasized (Chung et al. 1998; Claustre et al. 1999).

Both in vivo fluorescence and $a_{\phi}(676)$ are indices of the concentration of vegetal material (e.g., Lorenzen 1966; Bricaud et al. 1995), so that a covariation of both variables is

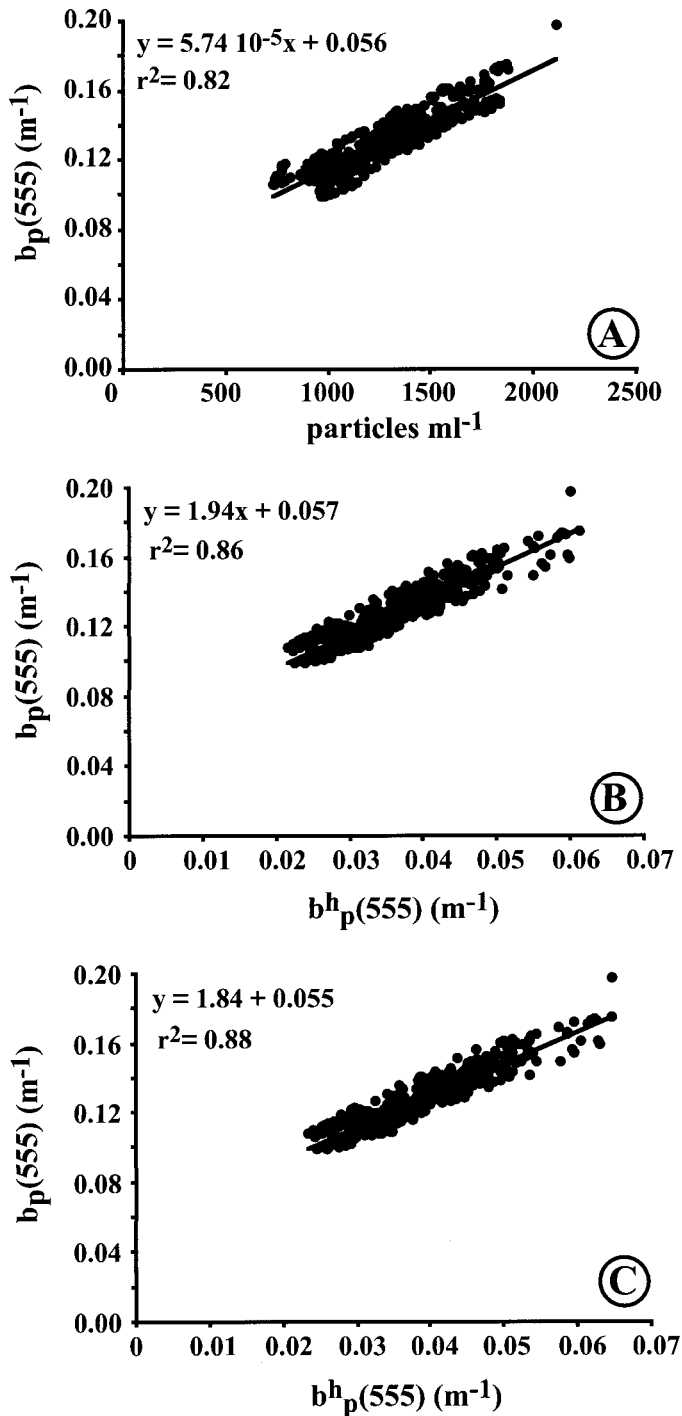


Fig. 7 Comparison between AC9-measured $b_p(555)$ and Hiac counter measured or derived quantities. (A) $b_p(555)$ vs. particle density. (B) $b_p(555)$ vs. $b^h_p(555)$. $b^h_p(555)$ is computed for particles in the size range 1.7–30 μm corresponding to that covered by the Hiac counter. (C) as in (B) except that the size range for $b^h_p(555)$ computation has been extended toward small particles (0.1–30 μm). See *Materials and methods for computational details*.

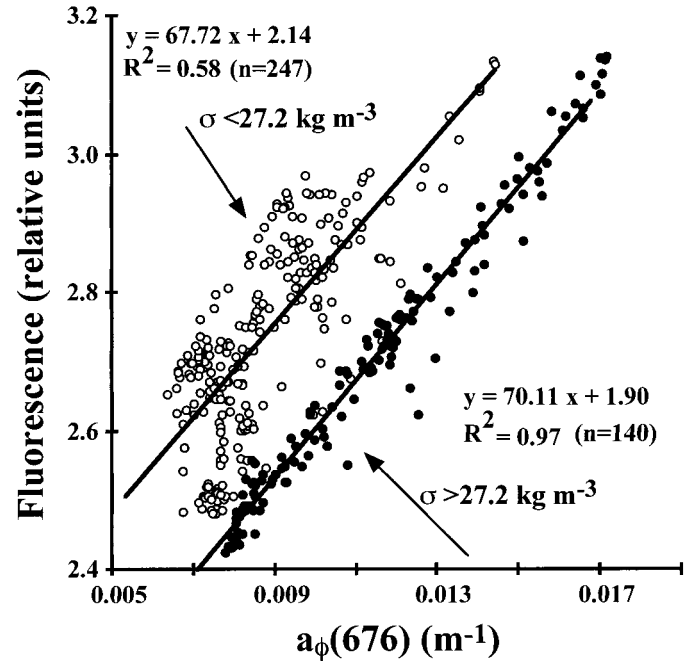


Fig. 8 Relationship between in vivo chlorophyll fluorescence and $a_\phi(676)$. The data set has been split into data corresponding to surface water density above (filled circles) and below (open circles) 27.2 kg m^{-3} .

expected. Figure 8, however, shows that a general relationship between both variables is not valid for the whole data set. Rather, a density cutoff of 27.2 kg m^{-3} (note that this limit corresponds to the density of the steps S1, S2, and S3; see Fig. 4) allows discrimination between two types of waters having specific fluorescence vs. $a_\phi(676)$ relationships. In the dense Mediterranean waters, the relationship is highly significant. In the less dense Atlantic waters, the relationship, although significant, is much more scattered. Moreover, the fluorescence/ $a_\phi(676)$ ratio, which is a rough estimate of the fluorescence quantum yield (mole emitted photons/mole absorbed photon), is higher for the less dense waters than for the denser ones (Fig. 8). These differences can be interpreted in two ways, which are not necessarily exclusive. First, red-fluorescing compounds such as phaeopigments (degradation products of chlorophylls), which were more abundant on the Atlantic than on the Mediterranean side (data not shown), as already observed during spring time (Claustre et al. 1994b), might add a background fluorescence to that of phytoplankton. A second explanation may be found in differences in the fluorescence quantum yields for Mediterranean and Atlantic phytoplankton populations; these differences could either result from variations in physiological states or in community structures. Although definitive evidence is lacking, it will be shown below that the vegetal peaks on the Mediterranean side present a large contribution of diatoms, while the vegetal peaks on the Atlantic side, having fluorescence/ $a_\phi(676)$ ratio 1.5 times higher than their Mediterranean counterparts, are flagellate dominated.

The nature of the particle assemblage—Along the transect, four situations, assumed as representative of the range

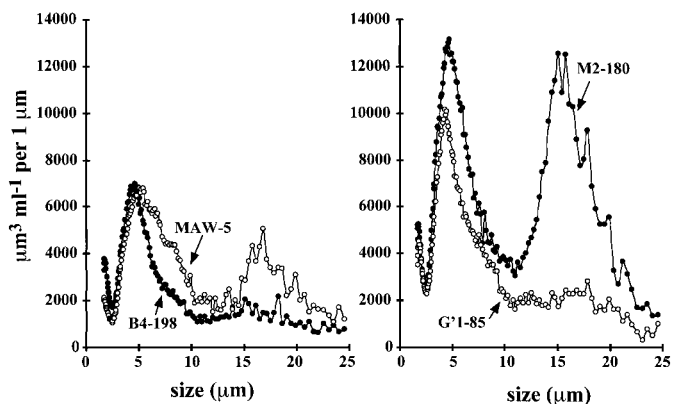


Fig. 9 Particle volume distribution for four representative situations encountered along the transect. MAW, B4, G'1, M2 refer to the density pattern defined in Fig. 4B (*see text*) and the following numbers (5, 194, 180, 85) correspond to the position (km from the beginning). For example, MAW-5 refers to samples taken in modified Atlantic waters at kilometer 5. These spectra represent an average of five consecutive spectra, corresponding to a horizontal resolution of ~ 2 km.

of qualitative and quantitative variations in the particulate biogenic material, have been selected for a more detailed analysis (*see Figs. 5, 6*): (1) the particle minimum at the beginning of the transect at kilometer 5 in modified Atlantic waters (MAW-5) [relative maximum in $b_p^*(555)$ and in the average particle size]; (2) the particle minimum associated with the density peak B4 at kilometer 194 (B4-194) [relative maximum in $b_p^*(555)$ and relative minimum in the average particle size]; (3) the particle peak at kilometer 85, at the base of G'1 (G'1-85) [minimum in average particle size and maximum in $b_p^*(555)$]; (4) the peak biomass in the Mediterranean waters at 180 km (M2-180) [relative maximum in average particle size and minimum in $b_p^*(555)$].

The particle size distribution displays common patterns for all situations (data not shown): superimposed on a regular decrease in particle number with increasing size, the distribution exhibits a maximum at about $3.5 \mu\text{m}$. In the upper ocean, such irregularities in the size distribution spectra, superimposed to an hyperbolic pattern, are generally considered to be the result of biological activity (e.g., Stramski and Kiefer 1991). To analyze such irregularities, the particle volume distribution function is more appropriate (Fig. 9): depending on the situation examined, one or two peaks in the volume distribution function are observed. The first volume peak is observed around $5 \mu\text{m}$ (plus or minus some variation) for all situations. The second peak, around $15\text{--}17 \mu\text{m}$, is observed for MAW-5 and especially for M2-180. These two volume maxima are likely indicative of flagellates (peak volume around $5 \mu\text{m}$) and diatoms (peak volume around $16\text{--}17 \mu\text{m}$). Indeed, a comparison between taxonomic pigment concentrations (fucoxanthin, marker of diatoms and $19'$ -hexanoyloxyfucoxanthin, marker of chromophyte flagellates) and the volume distribution spectra confirmed the respective belonging of flagellate and diatoms to these two distinct size classes for the area investigated during the cruise (Sciandra et al. in prep.).

When flagellates dominate the community, as in MAW-5,

G'1-85 and B4-194, the chlorophyll-specific scattering at 555 nm , $b_p^*(555)$ is high ($>0.45 \text{ m}^2 \text{ mg Chl } a^{-1}$) (Figs. 5, 6). In contrast, when the contribution of diatoms is high (e.g., for M2-180), $b_p^*(555)$ displays its lowest value ($\sim 0.20 \text{ m}^2 \text{ mg Chl } a^{-1}$) (Fig. 7). Such differences in $b_p^*(555)$ can be explained, on theoretical grounds, by a size effect: a $3.5\text{-}\mu\text{m}$ flagellate is 4.3 times more efficient in scattering than a $15\text{-}\mu\text{m}$ diatom (assuming that $n = 1.05$). Nevertheless, other factors might also be at the origin of the recorded differences in $b_p^*(555)$: lower chlorophyll content in flagellates than in diatoms, as well as the presence of heterotrophic flagellates or of coccolithophorids (especially their detached coccoliths), which contribute to scattering without contributing to $\langle \text{Chl} \rangle$. The possibility to monitor changes in nanoplanktonic assemblages (size, autotrophs vs. heterotrophs, presence of coccoliths) on the basis of variations in $b_p^*(555)$ is promising and should be explored in the near future to take full advantage of continuous bio-optical measurements (e.g., AC9).

Coupling–uncoupling between physical and bio-optical fields—In jet-front systems, the cross-frontal ageostrophic circulation, which is superimposed on the main geostrophic flow, is at the origin of the enhancement in primary production (Zakardjan and Prieur 1998, and references therein). Basically, this circulation is characterized by an upwelled flow on the heaviest part of the jet and a downwelled flow along the isopycnal slopes, on its lightest part. The upwelled flow is thought to transport “new” nutrients to the euphotic layer, which fuels production and allows high biomass to develop. The biogeochemical signatures of such a circulation have been reported in several cases (e.g., Prieur et al. 1993). For the Almeria-Oran front, in particular, the regular increase in the diatom biomass from the heavy to the light side of the jet was considered as a consequence of the enhancement of new production driven by cross-frontal circulation (Claustre et al. 1994b). The effects of cross-frontal circulation on surface biogeochemical fields are expected to be obvious only in the heavy part of the front, i.e., where upwelling takes place. Since downwelling occurs along isopycnal slopes, the frontal signature can be missed by surface sampling. Therefore, the present data set does not provide a general view of the biogeochemical response to the cross-frontal circulation. However, compared to previous studies, new information related to the dissolved matter, as well as a highly resolved description of the biogenic pools relative to the surface hydrological (density) fields, is afforded.

Dissolved material: CDOM is a byproduct of primary production (e.g., Bricaud et al. 1981), either directly through phytoplankton excretion during the growth phase (e.g., Lara and Thomas 1995), or indirectly through microbial breakdown of dissolved organic matter (Nelson et al. 1998). Increasing attention is being paid to CDOM dynamics in the ocean for two major reasons. (1) This pool is an important carbon reservoir, more than 20 times greater than the particulate organic matter pool (Lara and Thomas 1995); (2) it plays an important role in upper ocean processes, not only through its absorption of ultraviolet and subsequent protection of marine life (e.g., Blough and Green 1995) but also

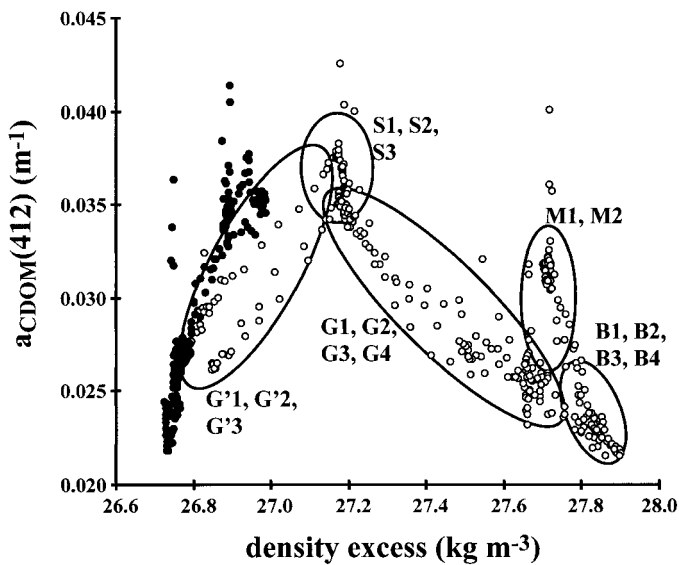


Fig. 10 Relationship between $a_{\text{CDOM}}(412)$ and density excess along the transect. The filled circle corresponds to the first part of the investigation in modified Atlantic waters (0–75 km, Fig. 6). Open circles correspond to the part of the transect that crossed the jet-front system several times (75–200 km, Fig. 7). The ellipses and the accompanying annotation refer to density patterns identified in Fig. 4B.

through its competition with phytoplankton for light absorption in the visible range (e.g., Babin et al. 1993).

In some situations, CDOM measurements can be used as a proxy for DOC concentration (Vodacek et al. 1997), allowing the mapping of DOC concentration by optical monitoring. Since CDOM is sensitive to photobleaching, the requirements for using CDOM as a proxy for DOC are low light levels and unstratified (or deeply mixed) waters (Vodacek et al. 1997). Such conditions were met in the present investigation. Observations were conducted during the winter (average daily radiation of 20 mole Quanta m^{-2}), the mixed layer was always >20 m, and the mixing was active, which was evidenced by quasi-homogenous vertical profiles of phytoplankton photoprotective index profiles (data not shown). These profiles can be used to trace the light history of phytoplankton in the mixed layer (e.g., Claustre et al. 1994a). Under the above conditions, the variations in $a_{\text{CDOM}}(412)$ can be interpreted, at least roughly, as variations in the DOC pool.

At the scale of the investigated area, Fig. 10 clearly highlights that the lightest as well as the heaviest waters have the lowest CDOM content. The abutting of these two water masses ends at the jet-front system whose CDOM content is generally higher, especially on the density steps. Because CDOM is a byproduct of primary production, we suggest that the CDOM enhancement associated with the frontal system is the consequence of the enhancement of biological production by frontal dynamics, which is in agreement with previous observations performed on this peculiar frontal system (e.g., Claustre et al. 1994b; Peinert and Miquel 1994).

At small scale, the present data set reveals that the CDOM pool is highly variable. Moreover, when compared to the

variations of the other biogenic materials studied here, CDOM presents, in general, the most reproducible features with variations in the density field (Fig. 6). Our present knowledge of physical/biogeochemical processes that could be at the origin of such patterns is not sufficient to propose definitive interpretation of such observations. Nevertheless, the density bumps (B), where minimal values in CDOM were recorded, are the expected signature of the upwelled flow (e.g., Zakardjan and Prieur 1998): since CDOM photobleaching can be neglected, the low CDOM content associated with these bumps likely traces the lack of biological activity, which is a further indication that these waters have only recently been brought to the surface layers. The presence of an enhancement CDOM zone associated with the density steps (S1, S2, S3) inside the jet (maximum eastern velocity) is rather surprising. This zone also corresponds to the highest percentage contribution of CDM to absorption [%CDM(412)] but to lowest values for particulate material [in particular, $a_{\phi}(676)$ (Fig. 6)]. Apparently, there is a decoupling between particulate and dissolved phases, which could be interpreted as a temporal decoupling between primary production rates and CDOM release across the jet-front system. Whether this CDOM (and detrital) enhancement (especially on the density steps) is a consequence of cross-frontal circulation remains to be investigated.

Particulate material: While CDOM dynamics are reproducible across the jet-front structure, this is not the case for particulate material. On the dense side of the jet-front system, two (B1, B3) of the four density bumps are characterized by a high particulate biomass (Fig. 6). In contrast, the two other bumps (B2, B4), which are flagellate dominated (e.g., Fig. 9, B4–194), are associated with low biomasses. Such opposite trends likely reflect differences in vertical velocities that are known to determine the biomass level in surface layers of such frontal environments (Zakardjan and Prieur 1998).

Along the density gradients G and G', no biomass maxima were observed. Again, this is likely due to the effects of cross-frontal circulation that are not obvious in subsurface layers, probably as a result of moderate vertical velocities (see Zakardjan and Prieur 1998). This assumption was confirmed by observations conducted at site 7 (explored just after the transect, Fig. 2) and located at the G4 gradient (Fig. 4): at 20 m, biomass maxima (diatom dominated) up to 5 mg Chl a m^{-3} were recorded, whereas at the surface, $\langle \text{Chl} \rangle$ was always low (<0.5 mg Chl a m^{-3}) (Oubelkheir et al. in prep.).

Two types of biomass maxima were recorded across the jet-front structure. At the very limit between the jet and the Mediterranean waters, where the eastern component of the velocity is minimal (Fig. 4), these maxima presented a high diatom contribution (e.g., M2–180, Fig. 9). In the jet core, where the velocity is maximal (Fig. 4), the biomass maxima were flagellate dominated (e.g., G'–85, Fig. 9). Diatoms are recognized as typical species of new production (e.g., Claustre 1994) and certainly drive the high particulate exportation flux in this frontal system (Miquel and Peinert 1994). This is not the case for flagellates, which in such frontal areas are considered as a transition community (Claustre et al. 1994b).

From the surface observations, it seems that two different systems are evolving on each side of the density steps. Such differences have potentially important consequences in terms of biogeochemical cycling in these areas.

Conclusions

The present study has pointed out small spatial changes in bio-optical and biogeochemical fields according to variations in surface density resulting from frontal dynamics. Owing to the novelty of the results presented here, a certain number of issues have not been fully resolved.

Particle density estimated by the Hiac counter and the scattering coefficient measured by the AC9 present remarkable covariation. However, the scattering budget attempted in this study ends at several interrogations. While some measurement errors cannot be discarded, part of the discrepancy between measured and computed scattering likely results from the poor knowledge (size distribution, relative index of refraction) about the small particles (living and detrital). Clearly, there is a need for a qualitative and quantitative characterization of this particulate pool to better address the role of the different particles in the range 0.2–20 μm in shaping the scattering coefficient.

CDOM remarkably covaried with the surface-density field. These variations trace the combined influence of water masses of different origin and of the biological activity. The complexity of the interaction between physical and biogeochemical processes at small scale prevented us from asserting definitive interpretation. Nevertheless, our results point out that this pool, long time considered as rather stable, is potentially a good tracer of water masses and of their biological activity. Investigations on sources (biological production) and sinks (photochemistry, kinetic of degradation) of CDOM are a prerequisite to further use this pool as a biogeochemically relevant tracer.

The results presented in this study were, at least partially, validated by nonsimultaneous measurements on discrete water samples. In the near future, such high-resolution measurements will probably develop with the generalization of the use of optical profilers. Nevertheless, these measurements, even if they appear self-sufficient, will require a suite of accompanying measurements aiming at cross comparing and validating the continuous results. Moreover, bio-optical monitoring only gives access to bulk variables. Therefore, a proper sampling strategy at a small or mesoscale will require the combination of continuous and discrete measurements. The former provides the range of variation of the bulk variables and does not miss events; the latter brings the necessary information on the detailed composition of the particle (or planktonic) assemblages.

The possibility to describe biogeochemical properties in a quasi-continuous mode is a fundamental result of this study and opens perspectives in bio-optical and biogeochemical modeling. Numerical models able to resolve mesoscale and submesoscale features (Zakardjan and Prieur 1998) are difficult to validate due to the scarcity of biogeochemical data at such scales. Therefore, bio-optical monitoring would be useful for providing the input fields and for validation pur-

poses. The present investigation deals only with surface measurements and is obviously an incomplete description of the biogeochemical fields associated with a frontal system. However, with the already available or forthcoming towed vehicle systems equipped with spectral profilers (Barth et al. 1998), two-dimensional or three-dimensional description of (bulk) biogeochemical fields is becoming a reality.

References

- BABIN, M., J.-C. THERRIAU, L. LEGENDRE, AND A. CONDAL. 1993. Variations in the specific absorption coefficient for natural phytoplankton assemblages: Impact on estimates of primary production. *Limnol. Oceanogr.* **38**: 154–177.
- BAKER, E. T., AND J. W. LAVELLE. 1984. The effect of particle size on the light attenuation coefficient of natural suspensions. *J. Geophys. Res.* **89**: 8197–8203.
- BALCH, W. M., K. A. KILPATRICK, P. HOLLIGAN, D. HARBOUR, AND E. FERNANDEZ. 1996. The 1991 coccolithophore bloom in the central North Atlantic. 2. Relating optics to coccoliths concentration. *Limnol. Oceanogr.* **41**: 1684–1696.
- BARTH, J., D. BOGUCKI, S. D. PIERCE, AND P. M. KOSRO. 1998. Secondary circulation associated with a shelfbreak front. *Geophys. Res. Lett.* **25**: 2761–2764.
- BISHOP, J. K. B. 1999. Transmissiometer measurements of POC. *Deep-Sea Res.* **46**: 355–369.
- BLOUGH, N. V., AND S. A. GREEN. 1995. Spectroscopic characterization and remote-sensing of non-living organic matter, p. 23–45. *In* R. G. Zepp and C. Sonntag [eds.], *The role of non-living organic matter in the earth's carbon cycle*. Wiley.
- BRICAUD, A., M. BABIN, A. MOREL, AND H. CLAUSTRE. 1995. Variability in the chlorophyll-specific absorption coefficient of natural phytoplankton: Analysis and parameterization. *J. Geophys. Res.* **100**: 13321–13332.
- , A. MOREL, AND L. PRIEUR. 1981. Absorption by dissolved organic matter in the sea (yellow substance) in the UV and visible domains. *Limnol. Oceanogr.* **26**: 43–53.
- , AND D. STRAMSKI. 1990. Spectral absorption coefficients of living phytoplankton and nonalgal biogenous matter. A comparison between the Peru upwelling area and Sargasso Sea. *Limnol. Oceanogr.* **35**: 562–582.
- BROWN, O. B., AND H. R. GORDON. 1974. Size-refractive index distribution of clear coastal water particulates from light scattering. *Appl. Opt.* **13**: 2784–2822.
- CHUNG, S. P., W. D. GARDNER, M. R. LANDRY, M. J. RICHARSON, AND I. D. WALSH. 1998. Beam attenuation and detrital particles in the equatorial Pacific. *J. Geophys. Res.* **103**: 12669–12681.
- CLAUSTRE, H. 1994. Phytoplankton pigment signatures of the trophic status in various oceanic regimes. *Limnol. Oceanogr.* **39**: 1207–1211.
- , P. KERHERVÉ, J.-C. MARTY, AND L. PRIEUR. 1994a. Phytoplankton photoadaptation in relation to some frontal physical processes. *J. Mar. Syst.* **5**: 251–265.
- , ———, ———, ———, C. VIDEAU, AND J. H. HECQ. 1994b. Phytoplankton distribution associated with a geostrophic front: Ecological and biogeochemical implications. *J. Mar. Res.* **52**: 711–742.
- , A. MOREL, M. BABIN, C. CAILLIAU, D. MARIE, J.-C. MARTY, AND D. VAULOT. 1999. Variability in particle attenuation and stimulated fluorescence in the tropical and equatorial Pacific: Scales, patterns and some biogeochemical implications. *J. Geophys. Res.* **104**: 3401–3422.
- DICKEY, T., AND OTHERS. 1998. Initial results from the Bermuda testbed mooring program. *Deep-Sea Res. I* **45**: 771–794.
- KITCHEN, J., AND J. R. V. ZANEVELD. 1990. On the noncorrelation

- of the vertical structure of light scattering and chlorophyll *a* in case I waters. *J. Geophys. Res.* **95**: 20237–20246.
- LARA, R. J., AND D. N. THOMAS. 1995. Formation of recalcitrant organic matter: Humification dynamics of algal derived dissolved organic carbon and its hydrophobic fractions. *Mar. Chem.* **51**: 193–199.
- LOISEL, H., AND A. MOREL. 1998. Light scattering and chlorophyll concentration in case I waters: A reexamination. *Limnol. Oceanogr.* **43**: 847–858.
- LORENZEN, C. J. 1966. A method for the continuous measurement of *in vivo* chlorophyll concentration. *Deep-Sea Res.* **13**: 223–227.
- MITCHELL, B. G., AND D. A. KIEFER. 1988. Chlorophyll-specific absorption and fluorescence excitation spectra for light-limited phytoplankton. *Deep-Sea Res.* **35**: 639–663.
- MOREL, A. 1973. Diffusion de la lumière par les eaux de mer. Résultats expérimentaux et approche théorique. *In* Optics of the sea, AGARD Lecture Series, 61, 3.1.1–3.1.76.
- . 1987. Chlorophyll-specific scattering coefficient of phytoplankton. A simplified theoretical approach. *Deep-Sea Res.* **34**: 1093–1105.
- , AND Y.-H. AHN. 1991. Optics of heterotrophic nanoflagellates and ciliates: A tentative assessment of their scattering role in oceanic waters compared to those of bacterial and algal cells. *J. Mar. Res.* **49**: 177–202.
- NELSON, N. B., D. A. SIEGEL, AND A. F. MICHAELS. 1998. Seasonal dynamics of colored dissolved material in the Sargasso Sea. *Deep-Sea Res. I* **45**: 931–957.
- PEGAU, W. S., D. GRAY, AND J. R. V. ZANEVELD. 1997. Absorption and attenuation of visible and near-infrared light in water: Dependence on temperature and salinity. *Appl. Opt.* **36**: 6035–6046.
- PEINERT, R., AND J.-C. MIQUEL. 1994. The significance of frontal processes for vertical particle fluxes: A case study in the Alboran Sea (SW Mediterranean Sea). *J. Mar. Syst.* **5**: 377–389.
- PETRENKO, A. A., B. H. JONES, T. D. DICKEY, M. LEHAITRE, AND C. MOORE. 1997. Bio-optical characterization of the particle field in Malama Bay, HI: Effluent and naturally occurring particles. *J. Geophys. Res.* **102**: 25061–25071.
- PRIEUR, L., C. COPIN-MONTÉGUT, AND H. CLAUSTRE. 1993. Biophysical aspects of “Almofront-1,” an intensive study of a geostrophic frontal jet. *Ann. Inst. Océanogr., Paris* **69**: 71–86.
- , AND S. SATHYENDRANATH. 1981. An optical classification of coastal and oceanic waters based on the specific spectral absorption curves of phytoplankton pigments, dissolved organic matter, and other particulate materials. *Limnol. Oceanogr.* **26**: 671–689.
- ROESLER, C. S., M. J. PERRY, AND K. L. CARDER. 1989. Modeling *in situ* phytoplankton absorption from total absorption spectra in productive inland marine waters. *Limnol. Oceanogr.* **34**: 1510–1523.
- SIEGEL, M. A., AND A. F. MICHAELS. 1996. Non-chlorophyll light attenuation in the upper ocean: Implication for biogeochemistry and remote sensing. *Deep-Sea Res. II* **43**: 321–345.
- STRAMSKI, D., AND D. KIEFER. 1991. Light scattering by microorganisms in the upper ocean. *Prog. Oceanogr.* **28**: 343–383.
- STRASS, V. 1990. On the calibration of large-scale fluorimetric chlorophyll measurements from towed undulating vehicles. *Deep-Sea Res.* **37**: 525–540.
- VIDUSSI, F., H. CLAUSTRE, J. BUSTILLOS-GUZMÁN, C. CAILLIAU, AND J.-C. MARTY. 1996. Rapid HPLC method for determination of phytoplankton chemotaxonomic pigments: Separation of chlorophyll *a* from divinyl-chlorophyll *a* and zeaxanthin from lutein. *J. Plankton Res.* **18**: 2377–2382.
- VODACEK, A., N. V. BLOUGH, M. D. DEGRANDPRE, E. T. PELTZER, AND R. K. NELSON. 1997. Seasonal variations of CDOM and DOC in the Middle Atlantic Bight: Terrestrial inputs and photooxidation. *Limnol. Oceanogr.* **42**: 674–686.
- ZAKARDJAN, B., AND L. PRIEUR. 1998. Biological and chemical signs of upward motions in permanent geostrophic fronts of the Western Mediterranean. *J. Geophys. Res.* **103**: 27849–27866.

Received: 29 March 1999

Accepted: 21 September 1999

Amended: 4 November 1999